

Effect of Additives and Annealing on the Performance of Nonfullerene-Based Binary and Ternary Organic Photovoltaics

Enas Moustafa, Alfonsina Abat Amelenan Torimtubun, Josep Pallarès,* and Lluís F. Marsal*

Fine tuning of blend morphology is a key factor that limits the performance of the bulk-heterojunction organic photovoltaics (BHJ-OPVs). Herein, the morphological control of the binary (PM6:Y7) and ternary (PM6:Y7:PC₇₀BM) blends is conducted through 1-chloronaphthalene (CN) solvent additive and thermal annealing (TA) treatment with respect to their influence on the photovoltaic performance. Moreover, a distinct study is accomplished on the optical and electronic properties of the treated and nontreated binary and ternary devices by external quantum efficiency measurements and impedance spectroscopy. The results indicate that these treatments affect the performance of the binary and ternary OPVs differently. Regarding the 2% CN addition, the current density of the binary devices is improved by $\approx 27\%$, whereas the fill factor of the ternary devices shows a pronounced increment of $\approx 22\%$. A contradictory behavior is exhibited by TA for the binary and ternary OPVs. The PCEs for binary devices (with/without CN) and 2% CN-treated ternary ones are improved, while diminishing the PCEs of the ternary ones with 0% CN. Accordingly, the highest efficiencies of the binary and ternary OPVs are obtained due to the dual effect of 2% CN solvent additive along with the TA treatments.

device physics.^[3,6,7] Moreover, this dramatic increase in the power conversion efficiencies (PCEs) was particularly due to minimizing the trade-off behavior between voltage loss and charge generation in NF-OPVs.^[8,9] This is attributed to the design of the central fused ring unit of these low-bandgap NFA molecules such as Y6 (BTP-4F) and Y7 (BTP-4Cl) with the virtue of their anisotropic structure.^[10–13] Moreover, they have the ability of tuning their energy levels and their strong absorption in the near-infrared region with the donor polymers.^[11,13–15] These properties lead to barrier-less free charge generation, low charge trapping, and high charge mobilities of the corresponding devices.^[16] These great advantages provide efficient ways to improve the performance of the NF-OPVs.^[9,11]

Furthermore, the bulk morphology of the photovoltaic active layer directly influences the charge transfer and transport


mechanisms, making it one of the pronounced limiting factors for the performance of BHJ-OPVs.^[3,17,18] For instance, the insufficient hole transfer from Y6 to PM6 (PBDB-T-2F) limits the exciton decay that affects the cell performance, as described by Wu et al. due to morphology defects.^[19] This declaration reflects the possibility of enhancing the NF-OPV performance through the optimization of the morphology of the photoactive blend.

There are several strategies that have been investigated to tune the active blend morphology toward better film quality through controlling the miscibility between the donor and the acceptor, domain size, and donor/acceptor (D/A) phase separation. This, to secure sufficient exciton dissociation and improved charge transfer, results in superior performance of the OPVs.^[3,20–22] Some of these avenues concern the photoactive blend modification by solvent additives,^[3,23–25] thermal annealing (TA),^[18,26] and further posttreatments.^[1,25,27] Among these strategies, moderating the morphology by the construction of ternary and quaternary blends performing ternary and quaternary OPVs.^[12,14,28–30] Regarding the first approach, 1-chloronaphthalene (CN) has been the most reported solvent additive to fine tune the morphology of PM6:Y6 OPVs, achieving 15.7% efficiency as compared with its nonadditive ones (15%), as presented by Lv et al.^[3] Furthermore, the influence of TA and posttreatments was significant in

1. Introduction

The inception of merging nonfullerene acceptors (NFAs) by replacing the fullerene counterpart in organic photovoltaics (OPVs) has pushed the bulk-heterojunction (BHJ)-based photovoltaics to achieve efficiencies approaching 20%.^[1–5] This reflects the tremendous attempts that have been conducted in the photoactive absorber material, interfacial device engineering, and

E. Moustafa, A. A. A. Torimtubun, J. Pallarès, L. F. Marsal
Department of Electric
Electronic and Automatic Engineering
Universitat Rovira i Virgili
43007 Tarragona, Spain
E-mail: josep.pallares@urv.cat; lluis.marsal@urv.cat

 The ORCID identification number(s) for the author(s) of this article can be found under <https://doi.org/10.1002/solr.202100480>.

© 2021 The Authors. Solar RRL published by Wiley-VCH GmbH. This is an open access article under the terms of the Creative Commons Attribution-NonCommercial License, which permits use, distribution and reproduction in any medium, provided the original work is properly cited and is not used for commercial purposes.

DOI: 10.1002/solr.202100480

enhancing both the blend morphology and the interface matching with the interfacial layers.^[18,31,32] As reported by Lui et al., they minimized the degree of energetic disorder and reduced the energy losses due to less nonradiative recombination of 0.17 eV, resulting in high PCEs up to 16.5%.^[31] For the second approach, introducing an additional component to the photoactive blend (ternary or quaternary) with careful selection leads to decrease in the density of trap states and increase in charge mobility.^[33–37] That has been observed in the ternary system through enhancing the fill factors (FFs), as reported by Gasparini et al.^[38] Furthermore, the ternary/quaternary blends influence the electronic energy-level alignment and the spectral coverage, which enhance photonharvesting, provide better charge transfer, and in turn improve the photovoltaic performance.^[5,15,37,39–41]

In our scenario, we demonstrate an interesting correlation between the CN solvent additives and the TA treatment on the optical and physical properties of the binary and ternary inverted NF-OPVs (iNF-OPVs) based on PM6:Y7 and PM6:Y7:PC₇₀BM active blend, respectively. Subsequently, we related the observed results with the photovoltaic performance of the devices. Our goal of the work is to manifest the diversity effect of these treatments on the binary (with NFAs) and ternary photovoltaic cells (with the addition of PC₇₀BM fullerene acceptor). Hence, we conduct a systematic investigation to reveal the effect of the mentioned treatments on the morphology of the binary and ternary blend layers. Moreover, a particular study was conducted on the electronic properties and the correlated charge transfer, separation, and recombination mechanisms using impedance spectroscopy (IS) and Mott–Schottky analysis of the treated and nontreated binary and ternary devices.

2. Results and Discussion

The effects of additives and TA treatment on the performance of binary and ternary iNF-OPVs were investigated by fabricating the device with the inverted structure of ITO/ZnO/active layer/V₂O₅/Ag, as shown in **Figure 1a**. ZnO and V₂O₅ were used as n-type and p-type charge transport interfacial layers, respectively; moreover, a binary BHJ of PM6:Y7 and a ternary blend of PM6:Y7:PC₇₀BM were used as the photoactive layer. The chemical structures of the PM6 polymer donor, Y7 NFA, and the PC₇₀BM fullerene acceptor with the energy-level alignment for binary and ternary devices are shown in **Figure 1b,c**, respectively. The energy positions of the band edges for the semiconductors and the metals' work functions were taken from other studies.^[42–44]

To better distinguish the parameters given, we labeled the binary iNF-OPVs in Roman capital letters A–D and the ternary iNF-OPVs in Arabic capital letters I–IV. As shown in **Figure 2**, Type A, B in binary iNF-OPVs, and type I and II in ternary iOPVs are the nonannealed (NA) devices treated without (0%) and with 2% v/v chloronaphthalene (CN) solvent additive, respectively. Moreover, type C, D in binary iNF-OPVs, and type III, IV in ternary iNF-OPVs are the thermal-annealed (TA) devices treated with 0% and 2% v/v CN, respectively. **Figure 3** shows the current density–voltage (*J*–*V*) characteristics of the fabricated binary and ternary iNF-OPVs with different processing treatments measured under illuminated AM 1.5G (100 mW cm^{−2}) conditions and in the dark. The photovoltaic parameters of the corresponding cells are shown in **Table 1**. As shown in **Figure 3a**, on the one hand, regarding the effect of CN additives, without TA treatment, device A (NA, 0% CN-pristine) exhibits a maximum PCE (PCE_{max}) of 8.26% with an average open-circuit voltage (*V*_{OC}) of 0.69 V, short-circuit current density (*J*_{SC}) of 21.23 mA cm^{−2},

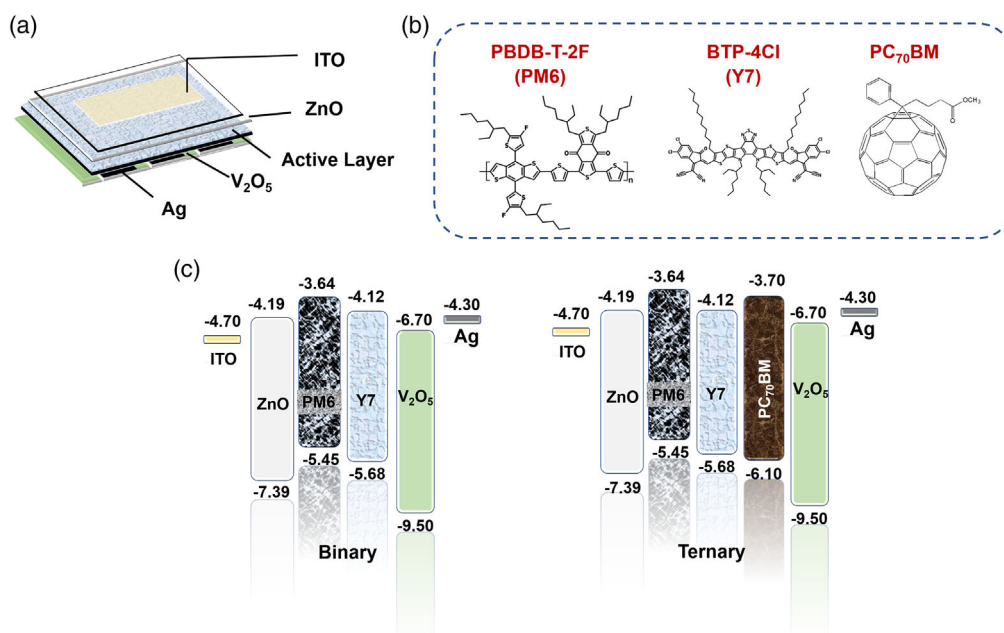


Figure 1. a) The schematic diagram of the fabricated iNF-OPV structure, b) the chemical structures of PM6-donor, Y7-NFA, and PC₇₀BM-fullerene acceptor, and c) the energy band diagrams of the inverted binary and ternary OPVs.

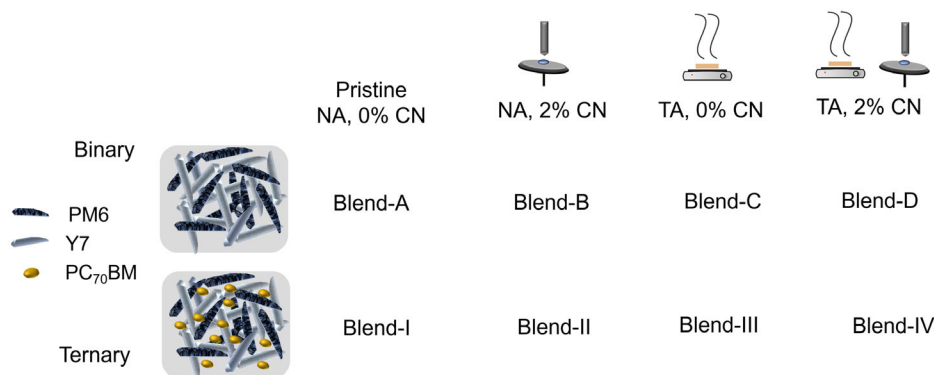


Figure 2. Schematic illustration of the nanomorphology models of the binary and the ternary BHJ films under different treatment conditions.

and FF of 0.56. After 2% CN additive, the device B's (NA, 2% CN) performance was improved to provide a PCE_{max} of 11.64% (with average $V_{OC} = 0.71$ V, $J_{SC} = 26.12$ mA cm⁻², and FF = 0.63). It can be clearly seen that the entire performance parameters of device B were enhanced upon the addition of 2% CN. Moreover, it was interesting to observe the same behavior for the thermally annealed C (TA, 0% CN) and D (TA, 2% CN) samples, where 2% of CN additives increases the PCE_{max} , average V_{OC} , J_{SC} , and FF from 10.09%, 0.74 V, 22.06 mA cm⁻², and 0.61, respectively, in device C to 13.62%, 0.75 V, 28.61 mA cm⁻², and 0.64, respectively, in device D. Furthermore, it is worth noticing that the J_{SC} values were highly pronounced by the CN additives, as shown in Figure 3a, for device B and device D, which may explain the improvement

in their PCEs. The enhancement of J_{SC} is in good agreement with the obtained external quantum efficiency (EQE) values and photocurrent charge carrier density versus effective voltage analysis, as discussed later. Another factor that assists the enhancement of the PCE comes from the increase of the FF due to the distinguished decrease in the series resistance average values (R_s) from 3.03 and 1.48 in device A and device C (with 0% CN), respectively, to 1.68 in device B and 1.20 in device D (with 2% CN). We obtained the same effect of improving the performance parameters upon 1% CN of the NA and annealed devices, as shown in Figure S1, Supporting Information.

In contrast, the obtained data remarked the effect of TA on the fabricated devices. By comparing device A with device C and device B with device D, we noticed that all the photovoltaics parameters

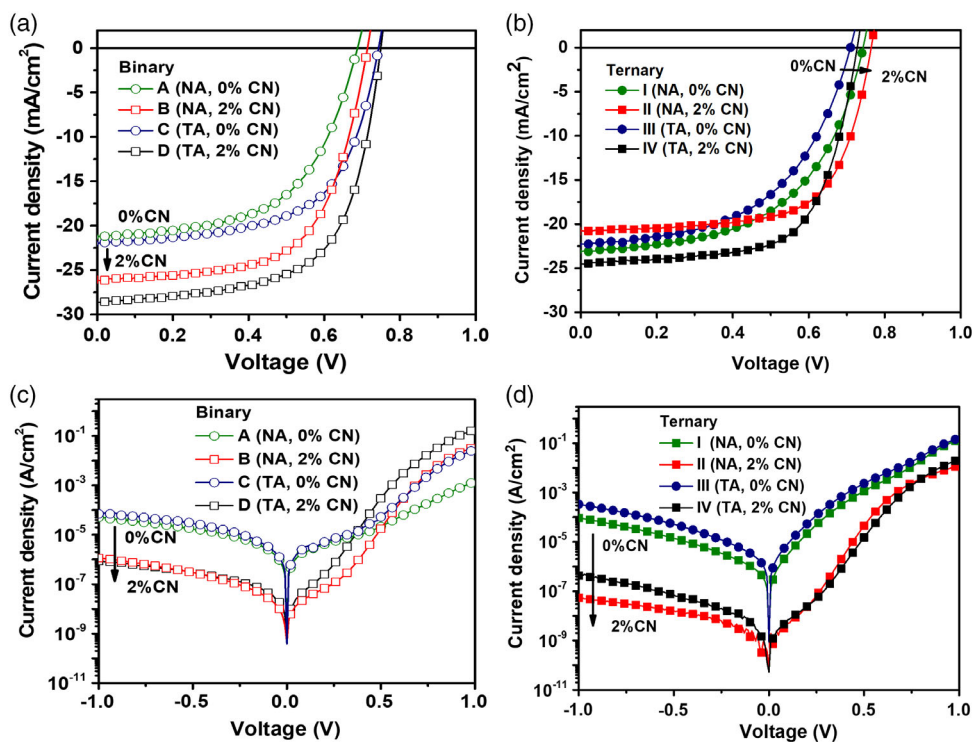


Figure 3. Current density–voltage (J – V) characteristic curves a,b) under AM 1.5 G illumination of binary and ternary iNF-OPVs and (c,d) in the dark of binary and ternary iNF-OPVs.

Table 1. Photovoltaic performance parameters statistics of the fabricated binary and ternary iNF-OPVs. The open-circuit voltage (V_{OC}), short-circuit current density (J_{SC}), FF, PCE, series (R_S), and shunt (R_{SH}) resistances presented from average of at least eight devices.

Device type	V_{OC} [V]	J_{SC} [mA cm^{-2}]	FF	PCE [%]	PCE_{max} [%]	R_S [$\Omega \text{ cm}^2$]	R_{SH} [$\Omega \text{ cm}^2$]
Binary							
A (NA, 0% CN)	0.69 ± 0.02	21.23 ± 1.18	0.56 ± 0.02	8.04 ± 0.22	8.26	3.03 ± 0.85	389 ± 22
B (NA, 2% CN)	0.71 ± 0.01	26.12 ± 1.62	0.63 ± 0.06	11.12 ± 0.52	11.64	1.68 ± 0.24	462 ± 32
C (TA, 0% CN)	0.74 ± 0.01	22.06 ± 0.74	0.61 ± 0.04	10.00 ± 0.09	10.09	1.48 ± 0.44	271 ± 12
D (TA, 2% CN)	0.75 ± 0.01	28.61 ± 0.43	0.64 ± 0.08	13.04 ± 0.58	13.62	1.20 ± 0.09	382 ± 57
Ternary							
I (NA, 0% CN)	0.74 ± 0.01	23.34 ± 0.93	0.54 ± 0.02	9.45 ± 0.70	10.38	1.69 ± 0.47	290 ± 34
II (NA, 2% CN)	0.76 ± 0.05	22.02 ± 1.29	0.63 ± 0.04	10.14 ± 0.92	11.16	2.09 ± 0.67	679 ± 259
III (TA, 0% CN)	0.71 ± 0.01	23.16 ± 1.08	0.52 ± 0.01	8.63 ± 0.54	9.05	1.49 ± 0.06	274 ± 33
IV (TA, 2% CN)	0.73 ± 0.01	23.54 ± 0.56	0.66 ± 0.01	11.28 ± 0.25	11.71	1.30 ± 0.02	650 ± 282

were enhanced but at the expense of slightly reduced R_{SH} values for the corresponding thermally annealed devices (device C and device D). However, the noticeable decline in the R_S average values of the thermally annealed samples (R_S of device C = $1.48 \Omega \text{ cm}^2$ and R_S of device D = $1.20 \Omega \text{ cm}^2$) might be the reason for enhancing the FF and in turn the PCEs of these cells. Furthermore, we can say that the major effect of TA was obtained by improving the FF and the V_{OC} of the TA cells (device C and device D). Though there was no clear effect observed due to the TA on the J_{SC} values of device C, it was more noticeable in device D. Accordingly, it is worth noting that device D illustrated the dual benefit of the 2% CN additives, as well as the TA, in fabricating efficient high-performance devices. Moreover, it was interesting to detect the same impact trend due to CN additives and TA using additional percentage of CN (1% v/v), along with various times of annealing (10 min and 30 min at 100°C), as shown in Figure S2, Supporting Information, and the obtained performance parameters statistics are shown in Table S1, Supporting Information.

As compared with the binary as-cast device type A, ternary as-cast device type I have a higher V_{OC} of 0.74 V, a higher J_{SC} of 23.34 mA cm^{-2} , and a slightly lower FF of 0.54, leading to a higher PCE_{max} of 10.38%. The higher V_{OC} and J_{SC} values in type I devices than those of type A device may arise from the contribution of PC₇₀BM as the third component in PM6:Y7-blend, improving energy alignment of the device as well as broadening the absorption window of the active layer, as discussed later. After 2% CN additive treatment, PCE_{max} of NA device type II increases to 11.16% with a higher V_{OC} of 0.76 V, a lower J_{SC} of 22.02 mA cm^{-2} , and a higher FF of 0.63. A similar behavior is observed for thermally annealed devices type III and IV in which the addition of 2% CN in ternary blend increases the PCE_{max} , V_{OC} , J_{SC} , and FF from 9.05%, 0.71 V, 23.16 mA cm^{-2} , and 0.52 for device type III to 11.71%, 0.73 V, 23.54 mA cm^{-2} , and 0.66 for device type IV. It is obvious that the overall photovoltaic parameters for the devices with and without TA treatment in either binary or ternary OPVs were enhanced upon the addition of 2% CN, suggesting that solvent additive is an effective strategy to improve device performance in different blend systems. Furthermore, it is worth noting that unlike binary OPVs with a noticeable increase in J_{SC} , ternary

OPVs show a noticeable increase in FF values upon the addition of 2% CN, as shown in Figure 3b. Highly pronounced FF values upon additive treatment originate from the apparent increase in R_{SH} from 290 to $679 \Omega \text{ cm}^2$ for NA devices type I and II and from 274 to $650 \Omega \text{ cm}^2$ for annealed devices type III and IV, respectively. Moreover, the difference of R_{SH} between devices type I and III and type II and IV in the ternary system is bigger than devices type A and C and type B and D in the binary system. It indicates that the solvent additive CN affect is more pronounced in FF for the ternary OPVs than the binary OPV counterpart. Furthermore, it was interesting to observe that J_{SC} values in binary OPVs are much higher than those of ternary OPVs upon additive treatment either for NA or TA devices, which contribute significantly to the enhancement of PCEs in binary than ternary OPVs. It also signifies that CN additive may play a different role to generate photocurrent in the presence of fullerene in the ternary system versus binary system.

In contrast, we observed a different behavior of the TA effect on the ternary devices compared with binary devices. In ternary OPVs, by comparing NA devices type I and II versus TA devices type III and IV, there is no significant difference observed in J_{SC} and FF values; however, we noticed a considerable decrease in V_{OC} values. It implies that the main effect of TA in ternary OPVs may be attributed to a change of different density of states (DOS) or energetic disorders of the blend due to the aggregation of fullerene upon TA.^[45,46] It is worth noting that TA treatment provides different behaviors between different blend systems in which V_{OC} in the binary system improves along with increase in J_{SC} and FF values upon TA, suggesting that in the other blend system, even small amount of addition of the third component may not give similar device performance parameters using the same treatment.

Figure 3c,d shows the $J-V$ curves in the dark for the binary and ternary devices, respectively. In binary OPVs, a lower leakage current under reverse bias was obtained for the 2% CN devices (device B and device D) than the 0% CN ones (device A and device C), as shown in Figure 3c. This lower leakage current in the 2% CN devices leads to increasing the shunt resistance R_{SH} ^[18] from 4.33×10^4 in device A to $3.80 \times 10^6 \Omega \text{ cm}^2$ in device B and from 2.34×10^4 in device C to $2.09 \times 10^6 \Omega \text{ cm}^2$ in device

D in the dark. This enhancement in the R_{SH} reveals a lower charge carrier recombination in the active layer blend.^[23] This behavior confirms the higher J_{SC} and FF observed for device B and D with 2% CN under illumination conditions, as shown in Figure 3a. In ternary OPVs, as shown in Figure 3d, similar behavior of lower leakage current was observed for 2% CN devices type II and IV compared with 0% CN device type I and III, leading to three-order-magnitude higher R_{Sh} from 6.42×10^4 and $2.15 \times 10^4 \Omega \text{ cm}^2$ to 3.08×10^7 and $2.00 \times 10^7 \Omega \text{ cm}^2$, respectively. A significant increase in R_{Sh} for 2% CN ternary devices validates the FF enhancement by the addition of 2% CN in the ternary system, as shown in Table 1. It is worth noting that ternary OPVs have higher R_{Sh} values than binary OPVs in 2% CN-treated devices, which is in good agreement with much lower leakage current possessed by ternary OPVs. At forward bias ($V > 0.3 \text{ V}$), we noticed a steep slope of the $J-V$ curves for binary TA devices (device C and device D) more than the NA cells (device A and device B) that indicates low- R_S ^[47] devices ($R_{S\text{-device A}} = 1188.1$, $R_{S\text{-device B}} = 47.53$, $R_{S\text{-device C}} = 59.19$, and $R_{S\text{-device D}} = 9.43 \Omega \text{ cm}^2$), which is in good agreement with the obtained R_S values under illumination, as shown in Table 1. In ternary OPVs, about one-order-higher R_S values of 117.47 and $79.22 \Omega \text{ cm}^2$ were observed for 2% CN devices type II and IV compared with 0% CN devices type I and III with R_S values of 12.61 and $10.30 \Omega \text{ cm}^2$, respectively. Interestingly, ternary OPVs have higher R_S values than the binary counterpart for 2% CN devices and vice versa for 0% CN devices. This behavior may be attributed to the interaction between the CN and fullerene acceptor in the active layer, leading to the increase in bulk resistance, and the other layer remained the same within the devices.

The dramatic increase in the J_{SC} for the binary OPVs with 2% CN-devices (type B and D) compared to that in 0% CN-devices (type C and D) as well as the trend of J_{SC} in ternary OPVs under different processing treatment were confirmed by the EQE response with AM 1.5G reference spectrum, as shown in Figure 4a,b, respectively. It can be noticed that the entire devices for both binary and ternary systems have similar wavelength ranges of broad photoresponse ranging from 300 to 950 nm. However, the absorption intensity at short wavelength range of 300–400 nm is still low due to the limited absorption of the polymer donor in this region.^[31,43] As shown in Figure 4a of the binary devices, the pristine devices (device A) show different responses than the other cells by a sharp reduction in the absorption range of 450–800 nm. This obtained reduction in the spectra was suggested to be related to the insufficient charge extraction and transport mechanism, which greatly matches with the device A's low performance parameters, as shown in Table 1. Otherwise, the EQE spectra from 450 to 800 nm exhibited strong photoresponses for the 2% CN devices with a maximum plateau achieving around 80% for the device B, around 90% for device D, and medium response at around 65% for device C with 0% CN. In the case of ternary OPVs, as shown in Figure 4b, as-cast device I have EQE values of 74.99% and 79.32% at 630 nm and 840 nm. The EQE values of 0% CN-device II at 630 nm slightly increase to 77.09%, whereas EQE values at 840 nm moderately decrease to 72.30% upon TA treatment, corresponding to a slight decrease in J_{SC} of 23.34 mA cm^{-2} for device I and 23.16 mA cm^{-2} for device III. After 2% CN addition, NA-device II shows the lowest EQE values of 75.34% and 72.01%, whereas TA-device IV displays the highest EQE values of 85.79% and 88.94% at the

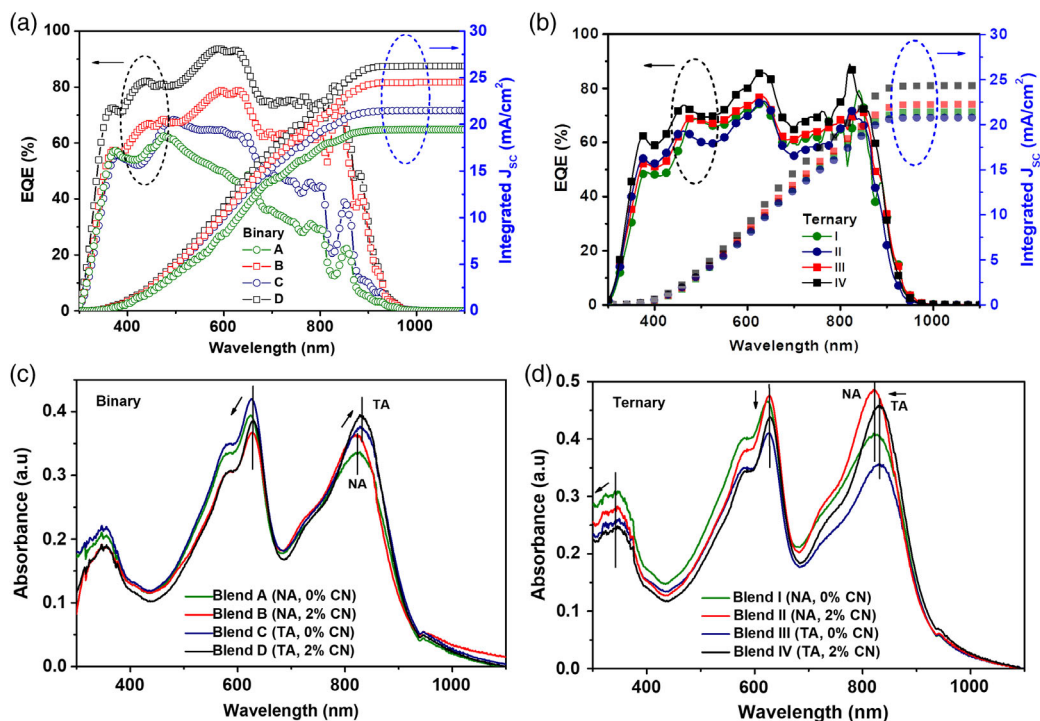


Figure 4. a,b) EQE spectra (left) and the integrated short-circuit current (right) of binary and ternary iNF-OPVs. c,d) UV(vis optical characteristics of the PM6:Y7 binary and PM6:Y7:PC₇₀BM ternary blend films under different treatment conditions.

wavelength of 635 and 820 nm, respectively, resulting in the lowest J_{SC} of 22.02 mA cm⁻² for device II and the highest J_{SC} of 23.16 mA cm⁻² for device IV among the studied ternary OPVs. It is interesting to see that the ternary 0% CN-devices have higher EQE values than binary 0% CN-devices, suggesting complementary absorption by the formation of the acceptor alloy of PC₇₀BM and Y7. However, lower EQE values of ternary 2% CN-devices than that of binary 2% CN-devices in the long wavelength range indicate the inefficient charge dissociation and charge transport mechanism in ternary devices by the addition of 2% CN as discussed later. In addition, the calculated integrated J_{SC} values from the EQE spectra were 19.44, 24.74, 21.49, and 26.24 mA cm⁻² for device A, B, C, and D in the binary system and 21.39, 20.76, 22.22, and 24.29 for device I, II, III, and IV in the ternary system, respectively. These calculated J_{SC} agreed with the values obtained from the $J-V$ measurements under AM 1.5 G illumination with the maximum error values of less than 10% (Table 1).

To further determine the effect of CN additives and TA treatment on the underlying PM6:Y7 and PM6:Y7:PC₇₀BM films and investigate the relation toward improving the J_{SC} in the fabricated devices, we conducted the UV-vis absorption spectrum of the PM6:Y7 and PM6:Y7:PC₇₀BM pristine and treated blend films, as shown in Figure 4c,d. Compared with the pristine films of binary (A), PM6 shows almost unchanged absorption peak positions (500–750 nm) with 2% CN additive films. However, surprisingly, the main change appeared in the absorption intensity of PM6, where the 2% CN additives showed a bit lower absorption intensity than the 0% CN blends in the binary system. In contrast, Y7 peak position (700–900 nm) in binary blends shows 8 nm redshift from 826 to 834 nm (maximum peak) besides higher absorption peak intensity for the 2% CN-modified blends. These results indicated that the Y7 molecules showed more tight aggregation, which is typically ascribed to $\pi-\pi$ interactions,^[48] which provide more absorption from the Y7 acceptor that efficiently converted into photocurrent.^[49] As a consequence, Y7 gave the major pronounced effect within the blend than PM6 by providing higher J_{SC} , as well as better device performance for the 2% CN-modified cells. In addition, it is worth to mention that this behavior explains the enhancement of the EQE response of the 2% CN devices above 800 nm, more than the 0% CN ones. Similar results were obtained by Wang et al.^[48] Furthermore, a different behavior was observed for the TA binary blend; it was clearly seen that the absorption spectra intensity increased for the TA devices more than the NA ones in binary films. Device C showed a higher absorption intensity than device A (the same for devices D and B) for both PM6- and Y7-related peaks. Interestingly, the same behavior was exhibited from the calculated absorption coefficients of the binary blends, as shown in Figure S3a, Supporting Information. From the obtained absorption coefficients, one may assume that the contributions of light harvesting from the treated devices were higher than those absorbed by the pristine ones. Accordingly, the overall evaluation of the binary blend film UV-vis spectra and the absorption coefficient reflects that 2% CN additives and TA treatment have a positive influence on Y7 and PM6, respectively. Hence, the EQE spectra verify the paired improvement effect obtained from CN additives and the TA step by showing higher intensity for the

champion device D with 2% CN and TA treatment for binary devices.

In ternary systems, we noticed that the blends with 2% CN additives (II and IV) show a modest and substantial increase in absorption intensity for PM6 and Y7 region, respectively, but decrease in absorption intensity of PC₇₀BM region (300–400 nm) compared with that of 0% CN films (I and III). No spectra peak shift was observed for the ternary films with and without CN additive. The increase in absorption intensity indicates the further ordering of Y7 molecule and hinders the molecular order of fullerene PC₇₀BM in ternary blend simultaneously by the addition of 2% CN.^[50] In contrast, a lower absorption intensity in all PM6, Y7 and PC₇₀BM spectra was acquired by TA-treated films (III, IV) compared with NA-films (I, II). The effect of TA in ternary films was more pronounced in lower Y7 absorption intensity than NA ternary films and it caused a 9 nm redshifted peak position from 820 nm to 829 nm for NA-films to TA-films. The redshift in Y7 absorption peak of the TA-blend may be due to increase in the interfacial charge carrier concentration of Y7.^[51] It is worth noting that device II showed the higher absorption coefficient (Figure S3b, Supporting Information); however, it demonstrates the lowest photogenerated current (Table 1, Figure 4b). This behavior is not merely defined by the active layer absorption of blend II but also by dissociation and recombination at the interfaces between the blend and the electrodes within the device, as observed in the study by Jin et al.^[52] Furthermore, we calculated the internal quantum efficiency (IQE) (IQE = EQE/absorption of the active layer) of the binary and ternary devices to estimate the efficient charge collection from the devices within the active layer, taking into account the recombination losses that might take place in the devices.^[53] Figure S4a, Supporting Information, for the binary devices shows the highest IQE intensities obtained for 2% CN devices of B and D, which greatly match with their superior J_{SC} values (Table 1). Furthermore, the highest IQE response exhibited for the champion device D possessed the highest J_{SC} value. However in the case of ternary devices, it was interesting to observe that the IQE response of the entire devices was quite comparable (Figure S4b, Supporting Information), which in turn verifies the quite close J_{SC} values obtained for the ternary devices. However, the highest IQE response was observed for IV device with highest J_{SC} value. It is worth noticing that the IQE response for the binary devices was higher than the ternary ones, which explains the higher J_{SC} values obtained for the binary devices more than the ternary ones. Hence, this study explains the higher absorption obtained for the ternary blend films than the binary ones; however, the ternary OPVs obtained lower IQE and hence, lower current generated than the binary devices, which might be attributed to the recombination losses due to the addition of PC₇₀BM as claimed previously. Similar behavior of highest absorption intensity leading to the lower IQE was observed by type II ternary based blend film, resulting to the lowest J_{SC} .

To see the behavior of optical properties and the interfacial charge transfer efficiency of all blends, we measured their photoluminescence (PL) spectra. From Figure S5, Supporting Information, it is shown that the PL peak of all blends shifts to a lower energy or higher wavelength (about 650 nm) than those of the absorption peak (about 620 nm) in the wavelength window from 600 to 850 nm, corresponding to the PM6

characteristic. It indicates that the PL and absorption measurement in this study is reliable as this phenomenon occurs due to the relaxation state of electrons within the atoms of PM6 to the lower energy level and it can emit the photon. From the PL measurement itself, the quenching degree of PM6 is higher in the ternary blend than those in the binary blend. It is important to note that the device parameters are difficult to explain by merely using the optical measurements. There are other parameters that affect the final performance, as we observed in our manuscript by IS, Mott–Schottky analysis, and morphology analysis by atomic force microscopy (AFM). In PL measurement, it gives us information about the energy transfer from the donor to the acceptor. In the case of binary systems, devices B, C, and D have similar energy transfer, whereas the as-cast binary A has a different energy transfer, indicating that the TA and additive treatment have a positive effect for the energy transfer in binary devices. Meanwhile, in the case of ternary devices, the energy transfer of the four types of ternary devices I–IV is different from each other, indicating that the TA and additive treatment gave a significant effect on the energy transfer of ternary blends.

Furthermore, it was interesting to investigate the low J_{SC} , V_{OC} , as well as PCEs obtained by the 0% CN binary devices (A and C) by studying the optical properties of the blend film using Urbach's rule as follows^[31,54]

$$\alpha(E) = \alpha_0 e^{(E-E_b)/E_U} \quad (1)$$

where $\alpha(E)$ is the optical absorption coefficient, α_0 is the optical absorption coefficient at the band edge, E is the photon energy, and E_U is Urbach's energy. The E_U value represents the DOS distribution, which explains the energetic disorder in the molecular orbitals.^[54] Hence, the smaller E_U value corresponds to the abrupt band edge.^[31] The obtained results in Figure S6a, Supporting Information, show that the curves of the 0% CN exhibited two different slopes at the low-energy region of tail-state distribution, explaining the high disorder in these 0% CN cells.^[31] Moreover, this behavior proves that the 0% CN devices have more trap states than the 2% CN results in reducing their device performance (Table 1). Interestingly, this behavior confirms the dip intensity of the EQE response that appeared for the 0% CN devices (A and C) above 800 nm (Figure 4a). In addition, the calculated values of the E_U (in the inset of Figure S6a, Supporting Information) were quite close for all devices; however, they still have lower values for device B than device A and for device D than device C, reflecting the less disorder distribution in the B and D devices due to 2% CN additive modification. In ternary systems, as shown in Figure S6b, Supporting Information, there is only one slope observed and the E_U values are almost similar with the binary counterpart, even lower in the case of 0% CN-devices (I vs. A). It indicates that the addition of third component PC₇₀BM in PM6:Y7 blend can provide the formation of the free-trap device.

To further understand the reason for improvement in the performance of the iNF-OPVs prepared by 2% CN additives and the TA treatment, we have evaluated the recombination characteristics of the fabricated devices by measuring the dependence of J_{SC} and V_{OC} on the incident light intensity (P_{Light}). The equation that represents the relation between J_{SC} and P_{Light} is $J_{SC} \propto (P_{Light})^{S_1}$, where the power-law exponent S_1 close to 1 represents the

insignificant bimolecular recombination.^[9,55,56] Figure 5a,b shows the J_{SC} dependence on P_{Light} of the fabricated devices; we noticed the difference in the dependency behavior at low and high light intensities. At low P_{Light} ($< 1 \text{ mW cm}^{-2}$), the S_1 values for the entire devices both for binary and for ternary systems were almost the same (around 0.6–0.7 which is less than 1), which indicates a major effect of bimolecular recombination. However, a different attitude was observed for the S_1 values at high P_{Light} ($> 10 \text{ mW cm}^{-2}$) for binary A, B, C, and D devices, which are 0.810, 0.860, 0.927, and 0.998 and for ternary I, II, III, and IV devices, which are 0.826, 0.842, 0.809, and 0.947, respectively. We can see that for the binary system, the pristine devices (A–NA, 0% CN) suffer from the major effect of bimolecular recombination ($S_1 < 1$) than the other devices. In addition, device B (NA, 2%CN) possessed a higher S_1 value representing a bit less bimolecular recombination effect than device A. Concerning the thermally annealed devices, the S_1 value tends to 1 that is indicative of the lowest bimolecular recombination excited in devices C and D. However, we can mention that device D possessed the closest S_1 value to 1 due to the virtue of 2% CN additives, along with the TA effect, which highly matched its prior performance. Meanwhile, the device that suffers from bimolecular recombination in ternary OPVs is device II (NA, 2% CN), giving the lowest PCE among ternary devices (Table 1). It is worth noting that to obtain device performance that suffers less from bimolecular recombination in ternary systems, solvent additive can be a good strategy.

The measurement of V_{OC} as a function of P_{Light} helps to identify the presence of trap-assisted recombination.^[57,58] Hence, Figure 5c,d shows the logarithmic dependence of the V_{OC} on P_{Light} of the binary and ternary systems, which is represented by following diode equation.

$$V_{OC} \alpha S_2 \left(\frac{KT}{q} \right) \ln(P_{light}) \alpha n_{id} \left(\frac{KT}{q} \right) \ln(J_{SC}) \quad (2)$$

where n_{id} is the ideality factor of the diode ($n_{id} = S_2/S_1$), k is the Boltzmann constant, T is the temperature, and q is the elementary charge. When the value of n_{id} is close to 1, it indicates that bimolecular recombination is the main form of recombination in the OSC devices,^[59] whereas $n_{id} > 1$ explains the presence of the trap-assisted recombination mechanisms.^[56,60] The S_2 values in binary iNF-OPVs were calculated by fitting Equation (1) and obtaining values of 1.746, 1.296, 1.350, and 1.212 that give n_{id} values of 2.156, 1.507, 1.456, and 1.214 (at $P_{Light} > 10 \text{ mW cm}^{-2}$) for A, B, C, and D devices, respectively. However, we obtained n_{id} values higher than 1 for the 0% CN devices (A and C) than the 2% CN (B and C) ones. However, the n_{id} values were more close to 1 for the TA (C and D) devices than the NA cells (A and B). Accordingly, we suggested that the trap-assisted recombination was mitigated for the devices treated with the 2% CN as well TA devices. All these factors approve the enhanced FF as well as the PCEs observed in the B- and D-treated binary devices. Using the same equation, the S_2 values of 1.987, 1.293, 2.263, and 0.991 for device I, II, III, and IV in ternary iNF-OPVs can be calculated, giving n_{id} values of 2.405, 1.536, 2.797, and 1.046, respectively. The lower n_{id} values for 2% CN-treated devices II and IV can be attributed to a less concentration of traps in the bulk, resulting in higher FF values for these devices, as shown in

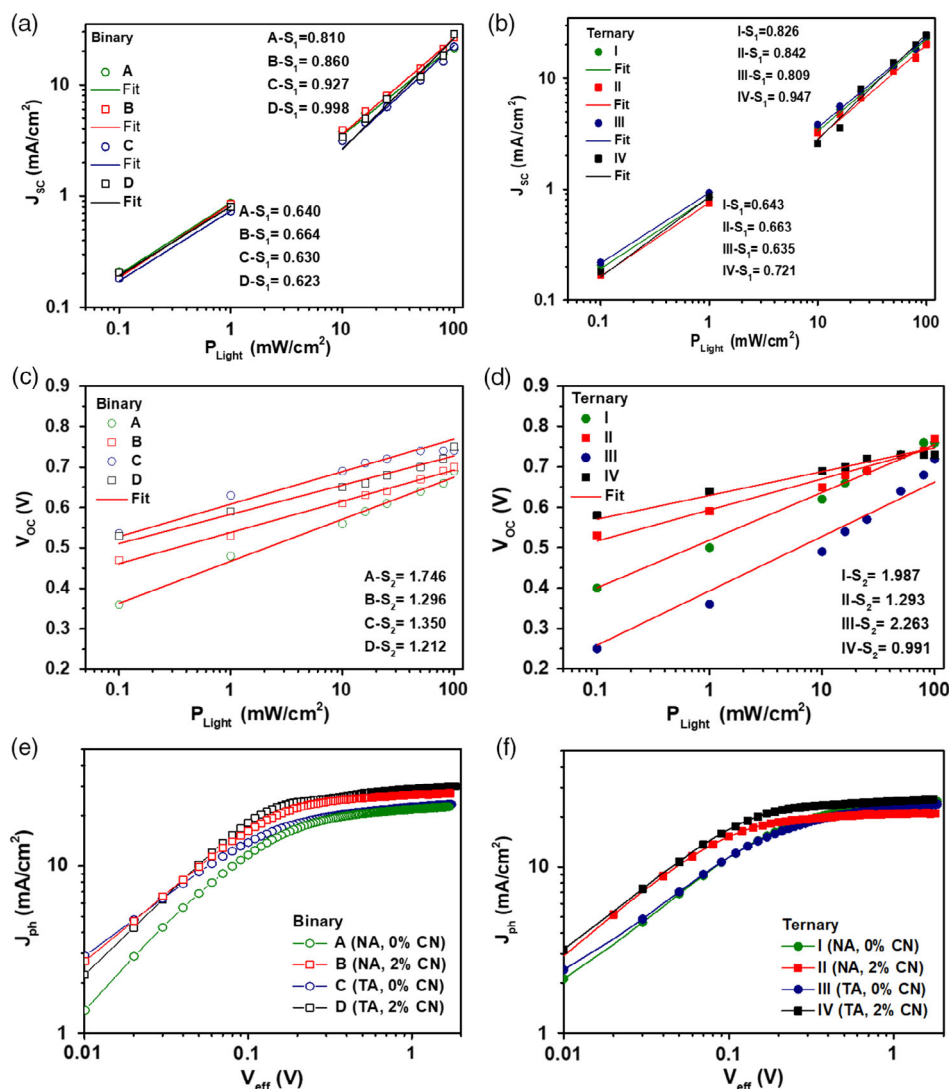


Figure 5. Binary and ternary device performance parameters of a,b) light intensity versus J_{sc} and c,d) V_{oc} . Symbols for the experimental data and the red line for the fitted data. e,f) J_{ph} versus V_{eff} characteristics of the binary and ternary devices under different treatment conditions.

Table 1. Surprisingly, the devices without additive (devices I and III) show n_{id} values higher than 2, which can be related to the energetic disorder of organic materials in the presence of the fullerene acceptor in PM6:Y7 blend due to nongeminate recombination.^[61]

Moreover, the dependence of the photocurrent (J_{ph}) on the effective voltage (V_{eff}) was calculated to evaluate the exciton dissociation probabilities (P_{diss}), maximum amount of absorbed photons that provides the dissociation and generation of free carriers (G_{max}), and the generation rate (G_{rat}) of the free charge carriers in the fabricated devices.^[62,63] J_{ph} is the difference between light (J_L) and dark (J_D) current density, $V_{eff} = V_O - V$, where V_O is the voltage when $J_{ph} = 0$ and V is the applied voltage.^[59,64,65] We evaluated the values of G_{max} , P_{diss} , and G_{rat} using the following equations.^[62,63,65,66]

$$G_{max} = J_{sat}/qL \quad (3)$$

$$P_{diss} = J_{sc}/J_{sat} \quad (4)$$

$$G_{rat} = P_{diss}/G_{max} \quad (5)$$

where J_{sat} is the saturation current density, q is the elementary charge, and L is the thickness of the blend film.

In Figure 5e,f, we plotted double logarithmic-scale curves of J_{ph} versus V_{eff} for binary and ternary OPVs, respectively. The obtained results exhibited that the J_{ph} of the devices increased linearly at low V_{eff} (<0.1 V). Then, it tends to saturate by increasing the $V_{eff} > 0.2$ V representing an efficient charge carrier separation.^[62] From the J_{sat} values extracted from Figure 5c,d, we can observe that the effect of 2% CN additives in both binary devices (B, D) and ternary devices (II, IV) has more sufficient charge carrier separation within the interfaces of the active layer blend^[59,62] than the 0% CN devices both in binary (A, C) and in ternary devices (I, III). However, the TA devices showed a higher

saturation behavior than the NA cells, but the effect of the 2% CN additives was more dominant than the TA effect. Table S2, Supporting Information, shows the optoelectronic parameters calculated from the $J_{ph} - V_{eff}$ curves. In binary systems, the values of the G_{max} for the NA devices A and B were 1.37×10^{28} and $1.66 \times 10^{28} \text{ m}^{-3} \text{ s}^{-1}$, respectively, which indicate that more sufficient free carrier generation and dissociation take place in device B due to the 2% CN additive. The same trend was achieved by the TA treatment, where the G_{max} of TA devices C and D were 1.40×10^{28} and $1.81 \times 10^{28} \text{ m}^{-3} \text{ s}^{-1}$, respectively. It is worthy to mention the highest value of G_{max} was that for device D, which consists of the highest J_{SC} . In turn, these observed results matched with the G_{rat} values (listed in Table S2, Supporting Information) for the devices which confirm that the photogenerated excitons efficiently dissociated into free carriers upon the 2% CN additive (device B) as well as TA ones (device D) which correlated with the corresponding performance of the devices (Table 1). Furthermore, P_{diss} of these devices followed the same trend of D (98.44%) > B (98.05%) and C (97.79%) > A (96.56%). Accordingly, the highest P_{diss} values correlate with the lower recombination observed for the device D-based NF-OPVs (Figure 5a,c), reflecting their high FFs, J_{SC} , and PCEs (Table 1). A different behavior from binary systems was observed in ternary systems where the CN additive treatment provides lower G_{max} values of $1.32 \times 10^{28} \text{ m}^{-3} \text{ s}^{-1}$ in NA-device II than that of $1.53 \times 10^{28} \text{ m}^{-3} \text{ s}^{-1}$ for NA-device I. In contrast, CN additive can provide higher G_{max} values of $1.56 \times 10^{28} \text{ m}^{-3} \text{ s}^{-1}$ in TA-device IV than that of III. This result is in good agreement with the trend of G_{rat} and J_{SC} values attained by device II and IV, showing the poorest and the highest free carrier generation and dissociation in ternary systems, respectively (Table 1, Figure 3b and 4b). It is worth mentioning that all P_{diss} values either for binary or ternary systems are above 90%, indicating the efficient exciton dissociation and charge collection in our fabricated devices.

The bulk surface morphologies of the binary PM6:Y7 and ternary PM6:Y7:PC70BM blend film ((pristine-NA, 0% CN), (NA, 2% CN), (TA, 0% CN), and (TA, 2% CN)) were investigated using AFM with morphology and phase modes, as shown in Figure 6. Interestingly, we observed two different trends regarding the effect of 2% CN additive and TA. First, for the NA films, where the addition of 2% CN increased the film roughness root mean square (RMS) from 2.88 and 1.31 nm (Pristine films—Figure 6a,e) to 3.67 nm and 1.35 nm (Figure 6b,f) and second and differently, for the TA films, 2% CN provides a more smooth film surface from RMS from 1.73 nm and 2.07 nm (Figure 6c,g) to 1.43 nm and 1.36 nm (Figure 6d,h). As compared with binary films, ternary films have smoother RMS values, especially for as-cast device and CN-treated devices, demonstrating that PC70BM can provide better mixing and smaller domain size on the blend morphology, which facilitate better charge transport; thus, high FF is obtained (see Table 1 and Figure 5 for device D vs. device IV).^[67,68] In binary films, the surface morphology in Figure 6a,c for 0% CN films reveals a strong aggregation in the film blend that commonly produces large phase separation domains that trap the exciton and hinder the charge transport.^[69] As a sequence, it affects the charge dissociation that leads to diminishing the J_{SC} and FF of the fabricated devices, as verified in devices A and C (Table 1, Figure 3a), which possessed

the highest leakage current (Figure 3c) and in turn lower PCEs. In case of device B, however, the 2% CN-based blend films (Figure 6b) showed higher surface roughness due to 2% CN additives than the pristine film A, but it demonstrates higher performance parameters than device A. Hence, we suggested that the 2% CN additive has the dominant effect on the physical properties of the film by decreasing the effect of Coulomb interaction with delocalization, as well as decreasing the domain size that leads to efficient separation of the excitons providing higher J_{SC} and better FF (Table 1) that make morphological roughness effects less pronounced.^[3,70,71]

Regarding the TA effect in binary films, the TA films showed a smoother homogenous surface for the 0% CN (Figure 6c) and 2% CN (Figure 4d) more than the NA blend films. A network of fiber with less-defined phase separations reflects the homogeneous mix of PM6 and Y7. This characteristics indicate the adequate inhibition of molecular aggregation due to the high thermal stability of the NFAs.^[18] Moreover, this behavior suppressed the carrier recombination and assisted the excitons in the active layer blend to reach the D/A interface, and in turn dissociated into free carriers,^[49] which typically contributed to enhancing the J_{SC} and FF of the devices. This obtained results are in line with device D, which has a lower RMS as well as more enhanced film crystallization (phase—Figure 6d). That likely facilitated the charge transport, which correlated with the closest n_{id} value to 1, highest P_{diss} (Figure 5e), lowest leakage current (Figure 3c), highest J_{SC} , FF, and PCE_{max} (Table 1). Accordingly, the tuning of both CN additives and TA steps are crucial for achieving the balance of exciton dissociation and charge collection, prompting better film morphology and increase in the PCE as confirmed by the case of device D.

To further investigate the impact of 2% CN additives along with the TA treatment step on the blend film surface, $C - V$ measurements were carried out on the fabricated devices in the dark, as shown in Figure 7a,b. Figure 7a shows the Mott–Schottky ($A^{-2}C^{-2} - V$) plots of binary devices A, B, C, and D; the built-in potential (V_{bi}) can be evaluated by the intercept of the curve with x -axis, as demonstrated in the figure. The obtained values of V_{bi} were 0.29, 0.39, 0.36, 0.43 V for devices A, B, C, and D, respectively. We noticed that the V_{bi} values were increased by 2% CN additives (devices B higher than A), as well as for the TA devices (D higher than C); hence, the lowest value was for the pristine A device (NA, 0% CN) and the highest value was for device D (2% CN and TA). Consequently, the low V_{bi} leads to low FF accompanied by diminishing the V_{oc} ,^[18] which is in line with the obtained values in device A and C (Table 1), confirming the reduction in the PCEs of these cells. It is worth mentioning that device D demonstrates a prior high chemical capacitance among the other OPVs, as shown in Figure 7a, due to the tuning of both 2% CN additives and TA treatment, resulting in less-localized states in the bandgap^[18] that lead to better V_{OC} and FF besides higher PCE.^[72] In the case of ternary iNF-OPVs, as shown in Figure 7b, a similar behavior was observed due to the addition of 2% CN, in which the V_{bi} values increase for 2% CN-devices II and IV (0.43 V and 0.49 V) compared with the 0% CN-devices I and III (0.39 V and 0.41 V). As observed for device I and III, at lower V_{bi} , the photovoltaic cells do not work efficiently as at forward voltages, the net field in the device reverses, thereby impeding charge carrier extraction

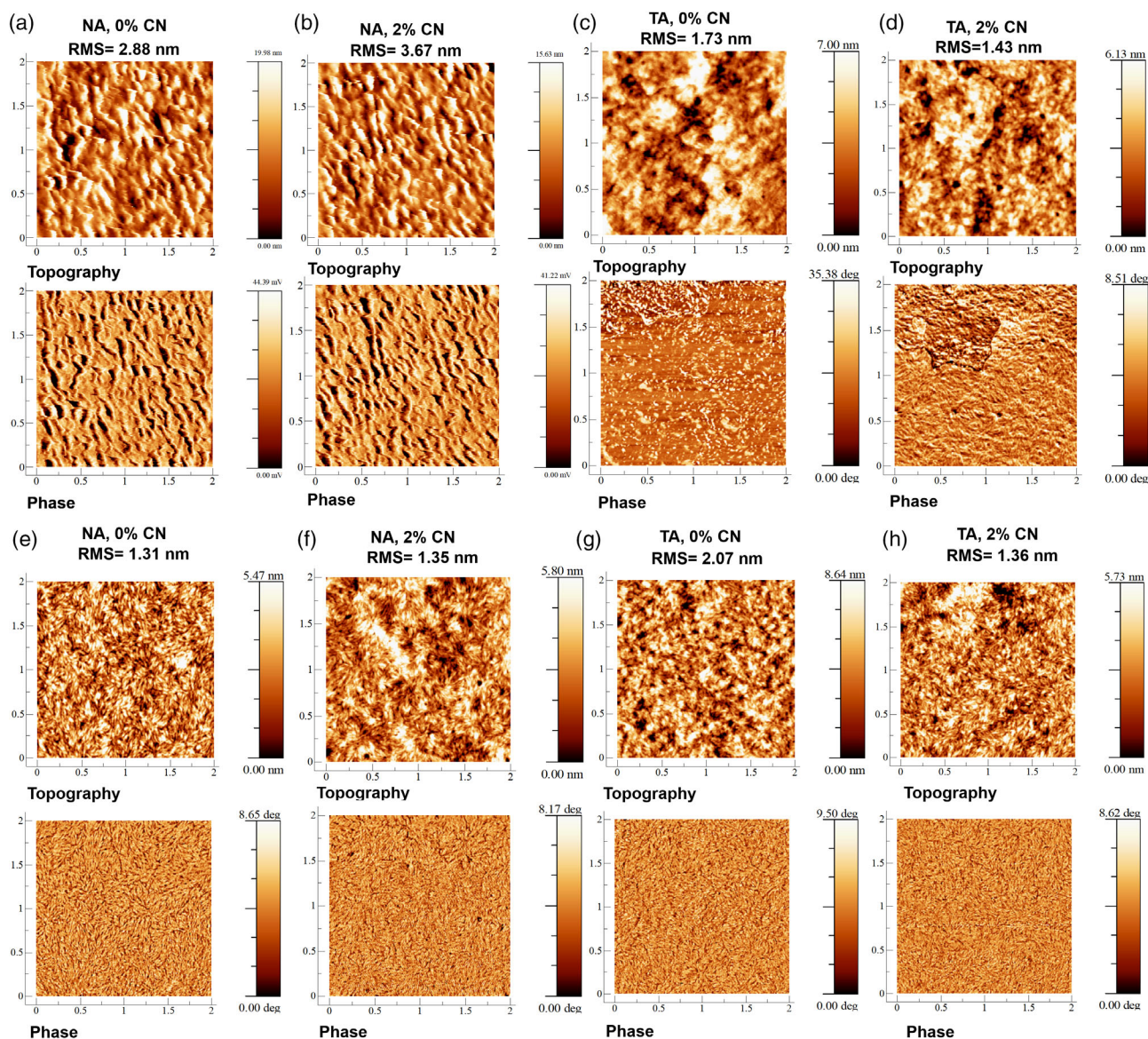


Figure 6. AFM topography and phase images of the binary PM6:Y7 and ternary PM6:Y7:PC₇₀BM blend films of a,e) pristine-NA, 0% CN, b,f) NA, 2% CN, c,g) TA, 0% CN, and d,h) TA, 2% CN.

instead of helping it. As a consequence, the devices with low V_{bi} can lead to low FF, as shown in Table 1 (devices I and III have lower FFs than devices II and IV). The results are in agreement with the observation from Upama et al.^[18]

IS measurements were carried out to gain more information about the electronic properties of the fabricated devices regarding the interfacial charge transfer and carrier recombination.^[73] Figure 7c,d shows the Nyquist plots for the binary and ternary fabricated devices at open-circuit bias voltage under illumination, which correlated with the efficient transfer at the active layer/electrode interface.^[73] The figure demonstrates a typical semicircle behavior with real part of impedance ($Z'(\Omega)$) as x -axis and imaginary part ($Z''(\Omega)$) as y -axis at open-circuit conditions. In the binary system, as shown in Figure 7c, we observed that

the 2% CN additive devices (B and D) showed a smaller arc radius than the 0% CN (A and C) ones. In addition, regarding the TA devices, devices C and D showed lower impedance and smaller arc radius than devices A and B, respectively. Furthermore, as Arredondo et al. proposed, the impedance arc at low frequency is an indication for charge accumulation that cannot be extracted by the contacts of the device.^[74] Hence, in Figure 7c, we can see that for the binary system, the low-frequency arc decreases by the addition of 2% CN as well as TA treatment, which is in the same line as the arc size. This behavior confirms the lower performance of device A (NA, 0% CN, Table 1) as it possesses the highest low-frequency arc which describes the more pronounced charge accumulation impact that could originate from the pristine morphology disorder of the

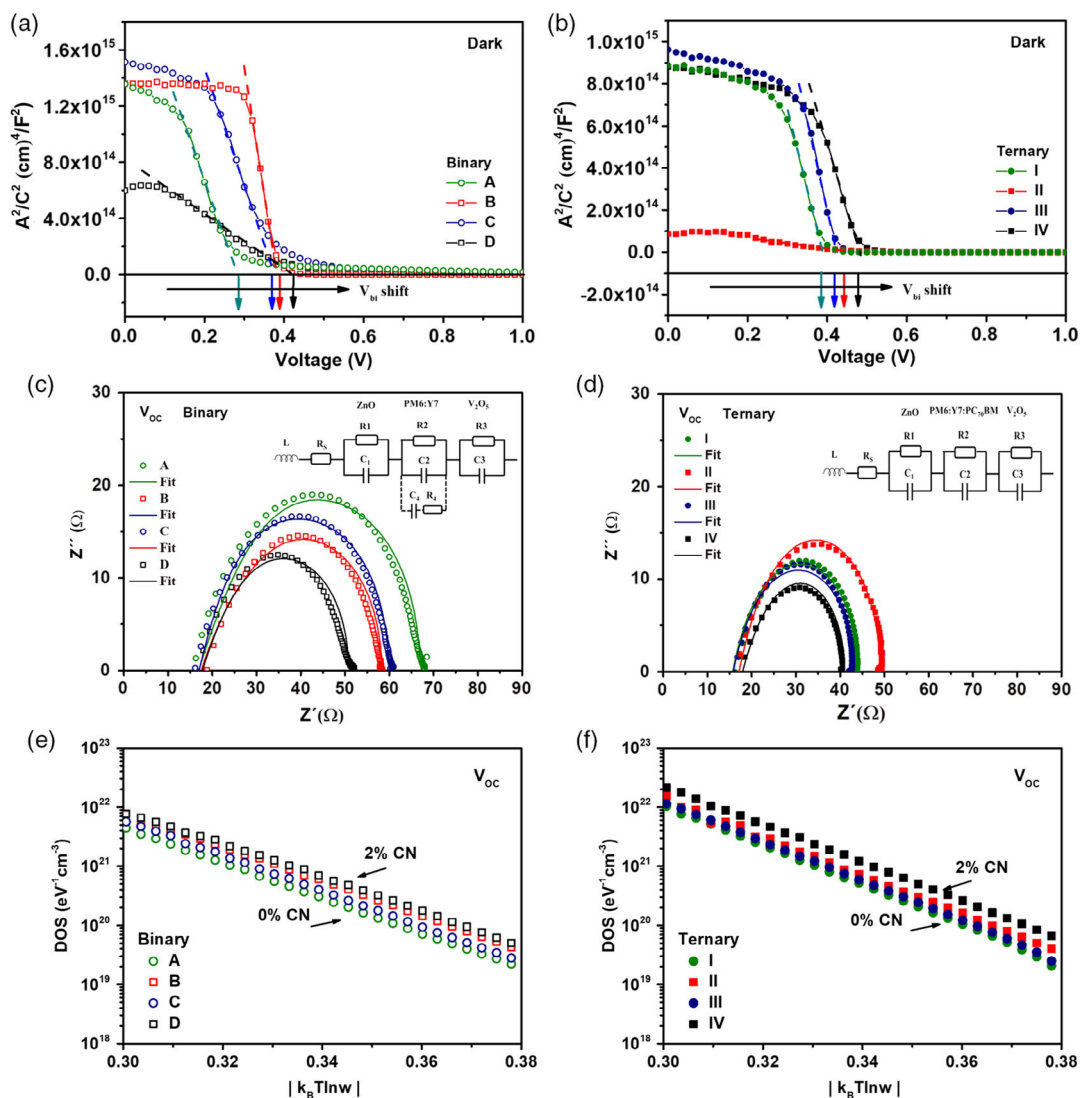


Figure 7. a,b) Mott(Schottky plot in the dark at 1 kHz of the binary and ternary iNF-OPVs. c,d) Nyquist plots at V_{OC} under AM 1.5 G illumination of the binary and ternary devices, using symbols for the experimental data and the fitting results in solid lines by applying the equivalent circuit in the inset of the figure. e,f) DOS as a function of $|k_B T \ln w|$ at V_{OC} under AM 1.5 G illumination of the binary and ternary iNF-OPVs.

blend.^[18] This consideration is correlated with the high leakage current and low V_{bi} of the pristine device A. On the other hand, for device D, which has the less low-frequency arc, reflecting the efficient charge extraction through the device results in lower leakage current, higher V_{bi} , and as a consequence, better device performance. Same behavior was obtained for the binary devices at maximum power point voltage (V_{mpp}) and short-circuit current (voltage = 0 V) in Figure S8a,b, Supporting Information. In the ternary systems, as shown in Figure 7d, the 0% CN-devices (I and III) have almost similar arc radius, whereas the 2% CN-devices (II and IV) have a totally different arc radius depending on the TA treatment given. It is interesting to mention that ternary devices have lower $Z' - Z''$ values than binary devices where the minimum Z' values seem to be similar but the maximum Z' values lower. It may correlate with the higher FF and better morphology for ternary than binary counterparts (Table 1) mainly due to the

higher R_{Sh} with similar R_s . Another observation in short-circuit conditions (Figure S8, Supporting Information) for ternary and binary devices is that the ternary devices have almost twofold higher $Z' - Z''$ values than binary devices. It indicates that binary devices show rapid charge extraction, whereas ternary devices show slower charge extraction, which contribute to the J_{SC} values of the devices and agree with the result from Table 1 and the optical analysis; J_{SC} of binary devices contribute more to the PCE enhancement. The PCE of ternary devices is mainly affected by the optical properties of the blend, wherein in this case binary shows a much higher PCE with TA and additive treatment, whereas the ternary devices show an inverse trend.

To get more information on the physical parameters of the fabricated cells, we conducted an electrical equivalent circuit to fit the experimental $Z' - Z''$ data. The electrical component used to fit the plot (solid lines) is shown in the inset of

Figure 7c for the binary devices and inset of Figure 7d for ternary devices. The fitted parameters are shown in Table S3, Supporting Information. The mentioned equivalent circuit consists of resistive/capacitive (RC) elements, where a distributed resistor (R) represents the resistance of electron transportation in each layer, where R_1 , R_2 , and R_3 refer to ZnO, blend active layer, and the V_2O_5 layer, respectively. In addition, C refers to the geometrical capacitance values of each layer, proving a parallel association of the resistor and capacitor for 3 RC elements in series. R_S represents the series resistance from the metallic wires and the ohmic components such as ITO layer Ag electrodes^[73,75] and L is the added inductor to fit the data at high frequency.^[73] It is important to mention that the model for the binary system composed of an extra implemented R_4C_4 in series, which is attached in parallel to R_2C_2 , corresponds the active blend layer obeying Debye's model.^[76] This model was the most suitable to fit the experimental data to explain the effect of the 2% CN additive and TA treatment conducted in the binary blend. This model considers the presence of a single type of trap created in one layer.^[76]

From the fitting data shown in Table S3, Supporting Information, we exhibited that the fitting capacitance values for each layer were in good agreement with the theoretical values shown in Table S4, Supporting Information. This might indicate that at V_{OC} , the IS data were controlled by the geometrical capacitances provided by the metal–insulator–metal (MIM) model reflecting the presence of fully depleted layers.^[77] From the fitted resistance values for each layer of the fabricated devices (Table S3, Supporting Information), it can be seen that the R_S value is low in all devices within the range of 2.0–3.0 Ω . First, by investigating the effect of 2% CN additives on the binary blend, we found that the R_2 values of device B (17.0 Ω) were less than that obtained in device A (22.0 Ω). In addition, device D showed R_2 value of 20.0 Ω , which is lower than the one of device C (25.0 Ω). Hence, 2% CN additives suppress the R_2 , leading to a better path for charge transportation within the blend film.^[73] Effects of additives in ternary R_2 values were quite opposite to the binary device in which ternary device II has higher R_2 values (15.0 Ω) than device I (10.0 Ω). In addition, device IV showed higher R_2 value of 15.0 Ω than device III (10.0 Ω). This result is in good agreement with the R_S values obtained from the dark J – V characteristic in which 2% CN-treated devices showed higher R_S values than 0% CN-treated devices (Figure 3d). Regarding the ZnO and V_2O_5 interfacial layer within binary and ternary devices, we revealed no clear effect upon the 2% CN additives in binary devices; however, a clear effect was observed in ternary devices. The ZnO and V_2O_5 interfacial layer in ternary devices upon 2% CN show higher R_1 and lower R_3 values than 0% CN, respectively. Thus, the total resistance (R_{Total}) evaluated for the devices (listed in Table S3, Supporting Information) was mainly controlled by the R_2 of the blend for binary device and R_1 of ZnO for ternary device. In binary devices, it followed the same trend of R_2 showing higher values for device A and C, verifying their low iNF-OPV performance and the smaller R_{Total} value for devices B and D, confirming the enhanced iNF-OPV performance. This trend of resistance obtained for the devices was confirmed by the Bode plot curve in Figure S7a, Supporting Information. Furthermore, this obtained behavior agreed with the R_S values obtained by the J – V characteristics under illumination (Table 1).

Second, as for the TA effect in the binary device, by comparing device A with C and device B with D, we showed that the R_2 values of the TA blends were a bit higher than NA films for both 0% and 2% CN devices, as shown in Table S3, Supporting Information. However, it was surprising that R_1 and R_3 for the interfacial layers (ZnO and V_2O_5) were clearly diminished, resulting in reducing the R_{Total} of the TA devices. This observation confirms the enhancement in the interface between the blend and the interfacial layers, which might be due to the homogenous film morphology obtained for the TA blend films as discussed previously. Hence, it was interesting to find that both 2% CN and TA treatments contributed in reducing the impedance of the fabricated devices, which might indicate less embedded traps in the related blend film that highly matched with the calculated n_{id} value observed for device D. In addition, these behaviors followed the same trend obtained in the previous discussed characteristics, confirming the enhancement effect upon combining multiple treatments. In ternary devices, again, a different behavior was observed upon TA. The TA-devices III and IV have lower R_1 for ZnO layer compared with that of devices III and IV; however, the same R_3 for V_2O_5 layer was observed. It is worth noting that the R_1 value of device II is the highest among ternary devices, which can be attributed to the lower quality of the interface between the blend and interfacial layers, as observed by AFM analysis in Figure 6e–h.

Though the best device performance was obtained by the binary system under combined treatments (device D, TA, 2% CN), except for the pristine devices (A, I), it is important to notice that the highest FF values were attained by ternary device IV (TA, 2% CN) due to the improvement of blend morphology by the addition of PC₇₀BM. This result is in good agreement with the lower Z' values measured for ternary systems. In addition, the experimental $Z' - Z''$ for ternary devices can be fit excluding the Debye model, that is, without including impeded trap effects. Therefore, the reason behind the best performance of binary OPVs was its high J_{SC} value related to its optical properties as well as a high dissociation probability.

An alternative way for understanding the recombination mechanisms using IS technique is the measurement of the capacitance–frequency (C – f) to calculate the trap DOS. This characterization was conducted for OPVs in many research works to obtain the change in trap emission and disorder-induced tail states within the devices.^[73,78–81] Therefore, the traps' DOS at a given energy level, E_{ω} , can be evaluated by the variation of the capacitance of the device with frequency. This correlated with the trapping and the charge release by shallow traps in the bandgap near the Fermi energy level, as explained by Equation (2).^[80,81]

$$DOS(E_{\omega})_{traps} = -\frac{V_{OC}\omega}{iqTk_B} \frac{\partial C}{\partial \omega} \quad (6)$$

where C is the measured capacitance, V_{OC} is the open-circuit voltage obtained by the J – V characteristics under illumination conditions, ω is the angular frequency, t is the layer thickness, k_B is the Boltzmann constant, q is the electron charge, and T is room temperature (300 K).

To observe the relation of the trap DOS as an energy dependent, the following equation has been applied.

$$(E_{\omega})_{\text{traps}} = k_B T \ln \frac{2\beta N}{\omega} = E_O - k_B T \ln \omega \quad (7)$$

where β is the cross section and N is the effective DOS.^[82] Since assuming that $2\beta N$ is independent of the frequency value, the change in its value is related to the shift in the DOS values on energy scale (E_O).^[75]

Figure 7e shows the calculated trap DOS plotted as a function of energy for the fabricated binary devices. It shows a single exponential trap distribution for all samples, where almost same slope values were detected, which define the same trap activation energy and carrier response.^[83] Regarding TA treatment, we did not see much change in the DOS value from device A to C or from B to D. However, a shift in E_O value was observed, showing higher DOS of B and D devices with 2% CN more than device A and C with 0% CN. This behavior can be explained by Equation (3), assuming that this small shift of E_O or higher DOS values might result from the decrease in the βN value, which means higher obtained energy because of less-localized shallow trap sites created due to the addition of 2% CN to the blend film.^[75,81,82,84,85] The details regarding the calculation of the energy shifting values are explained in the Supplementary Information. By comparing the energy shift values of the 0% CN devices (A and C) and the 2% CN ones (B and D), as shown in Figure S9a,b, Supporting Information, we obtained that the 0% CN devices exhibited almost double trapping sites more than the 2% CN-treated ones. This observation confirms the superior performance of the B and D devices due to the addition of 2% CN that diminished the presence of defects inside the devices. This behavior was interestingly highly matched with the E_U study discussed previously in Figure S6a, Supporting Information, and with the impedance behavior in Figure 7c along with the performance obtained in Figure 3a, which explains the higher FF, V_{OC} , and J_{SC} obtained for these binary devices. Similar behavior was noticed with ternary devices, where the same trap activation energy observed by almost same slope values for 0% CN-devices (I, III) than 2% CN-devices (II, IV), as shown in Figure 7f. Hence, ternary devices manifested higher trap states distributed in the 0% CN devices than the 2% CN cells, as presented by the energy shifting values in Figure S9c,d, Supporting Information, which matched with the device performance obtained for I and III OPVs. Furthermore, like binary devices, TA-treated (III, IV) and NA-treated (I, II) ternary devices also show insignificant change in the DOS values. However, higher DOS values were observed for ternary devices compared with binary devices.

Regarding the previous discussed characteristics, we conclude that the 2% CN possessed the major effect on the performance of the binary and ternary devices, especially for the J_{SC} and FF parameters, respectively. In addition, TA treatment assisted the improvement of blend morphology, resulting in higher V_{OC} and FF along with the PCE in binary blend, whereas TA treatment in ternary devices can be effective with the addition of 2% CN.

3. Conclusion

In summary, we investigated the role of the CN solvent additive and TA treatment on the high-performance NF-based binary and ternary OPVs. Two different blends, binary PM6:Y7 and

fullerene-added ternary PM6:Y7:PC₇₀BM, were comparatively studied. We found that the solvent additive improves the performance for both binary and ternary iNF-OPVs by superior enhancement in the J_{SC} and the FF of the devices, respectively. An improvement in J_{SC} values is noticed in the binary system mainly due to its high EQE values and high dissociation probability. In addition, an increase in FF values for ternary devices is in good agreement with the lower Z' values measured, and the experimental $Z' - Z''$ for ternary devices can be fit excluding the Debye model, that is, without including interface trap effects. Furthermore, an opposite behavior was observed by applying TA treatment for binary and ternary iNF-OPVs, in which TA treatment provides a higher PCE for binary iNF-OPVs mainly due to the increase in V_{OC} . Thus, the dual role of additive and TA treatments is beneficial for improving the binary device performance. In contrast, TA treatment plays a different role in ternary iNF-OPVs, where without the addition of CN, TA treatment aggravated the performance due to PC₇₀BM aggregation upon TA, whereas with the addition of CN, TA treatment plays a dual role with CN by further increasing device performance probably due to the high-boiling-point CN additive to help balance the aggregation of PC₇₀BM. Hence, the study highlights the significance of solvent additive and TA treatments on the active layer morphology and its consequence to device performance. The process engineering demonstrated in this work can be useful in optimizing the NF-based photovoltaics by taking into account that even small amount of third component may not give similar device performance parameters using the same treatments.

4. Experimental Section

Materials: PM6 (poly[2,6-(4,8-bis(5-(2-ethylhexyl-3-fluoro)thiophen-2-yl)benzo[1,2-b;4,5-b']dithiophene))-alt-(5,5-(1',3'-di-2-thienyl-5',7'-bis(2-ethylhexyl)benzo[1',2'-c;4',5'-c']dithiophene-4,8-dione)) polymer donor and Y7 (2,2'-((2Z,2'Z)-((12,13-bis(2-ethylhexyl)-3,9-diundecyl-12,13-dihydro-[1,2,5]thiadiazolo[3,4-e]thieno[2'',3'':4',5']thieno[2',3':,4,5]pyrrolo[3,2-g]thieno[2',3':4,5]thieno[3,2-b]indole-2,10-diy))bis(methanylylidene))bis(5,6-dichloro-3-oxo-2,3-dihydro-1H-indene-2,1-diylidene))dimalononitrile) NFA was purchased from One-Material Inc. The fullerene acceptor PC₇₀BM ([6,6]-phenyl-C₇₀-butyric acid methyl ester) was supplied from Solenne BV. 1-chloronaphthalene (CN) solvent additive was obtained from Sigma-Aldrich. Zinc acetate dehydrate was obtained from Sigma-Aldrich. Vanadium oxide (V₂O₅) and high-purity silver (Ag) wire (99.99%) were purchased from Sigma-Aldrich and Testbourne Ltd., respectively.

Device Fabrication: The NF-OPV devices were fabricated in an inverted structure of ITO/ZnO/active layers/V₂O₅/Ag. The indium tin oxide (ITO)-coated glass substrate with the sheet resistance of 10 Ω cm⁻² was cleaned with deionized water/detergent and then sonicated in acetone, methanol and isopropanol solution in a sequence for 10 min, respectively. The cleaned ITO-glass substrates were dried under nitrogen stream and transferred to an oven for 10 min at 100 °C. Before fabrication, the substrates were treated in UV-ozone for 15 min to remove any organic residues and activate the ITO surfaces. The zinc oxide (ZnO) precursor was prepared by sol-gel method according to our previous work.^[75,86] Zinc acetate dihydrate 150 mg was dissolved in 1 mL of 2-methoxyethanol with 30 μL ethanolamine; then, the mixture was left for 1 h under vigorous stirring at 70 °C and was diluted by methanol in 1:1 (v/v) ratio to obtain ZnO precursor solution. The ZnO precursor solution was spin coated on top of the precleaned ITO substrates at 4000 rpm for 40 s and then annealed in air for 1 h at 200 °C. The ZnO-coated ITO substrates were brought to a nitrogen-filled glove box for active layer deposition. The binary PM6:Y7

blends with the weight ratio of 1:1 were dissolved in chlorobenzene to prepare the total concentration of 20 mg mL⁻¹ solution. The ternary PM6:Y7:PC₇₀BM blends with the weight ratio of 1:1:0.1 were dissolved in chlorobenzene to obtain the total concentration of 20 mg mL⁻¹ solution. All blend solutions were stirred and heated on a hotplate at 80 °C for 3 h. Different concentrations (from 0 vol% to 2 vol%) of 1-chloronaphthalene were added as the solvent additives before device fabrication to study the effect of addition of the additives for all blends. The blend solutions were spin coated onto the ZnO/ITO substrates to obtain an active layer thickness of around 100 nm. Then, the prepared films were treated with and without TA at 100 °C for 1 h to study the effect of TA treatment on the performance of the binary and ternary solar cells. The substrates were finally transferred into an evaporation chamber inside the glove box where 5 nm of V₂O₅ and 100 nm Ag were sequentially deposited under high vacuum conditions ($\leq 1 \times 10^{-6}$ mbar). The V₂O₅ layer was deposited at a rate of 0.05 kÅ s⁻¹ and the Ag film rate was 0.1 kÅ s⁻¹ for the initial 10 nm thickness and then increased to 0.4 Å s⁻¹ till 100 nm film thickness that was conducted through 190 min.^[87] This slow rate of evaporation was conducted to provide a smoother interface in addition to avoid the degradation that might happen to the V₂O₅ thin layer during Ag deposition. The effective area of devices was 0.09 cm².

Device Measurement and Characterization: The current density–voltage characteristics, namely, the short-circuit current density (J_{SC}), open-circuit voltage (V_{OC}), FF, and PCE, were extracted using a Keithley 2400 Source Measure Unit with a solar simulator (Abet Technologies model 11000 class type A, Xenon arc) as an artificial light source. The standard light intensity of the AM 1.5G spectrum was calibrated by an NREL-certified monocrystalline silicon photodiode. The devices were tested under illumination at light intensity of 100 mW cm⁻². Moreover, dark measurements were carried out to obtain J – V dark curves. All the J – V characteristics were conducted at room temperature. J – V curves were measured in the forward direction from –1 to 1 V, with a scan step of 0.01 V. V_{OC} and J_{SC} over different light intensities were obtained by J – V measurements under the solar simulator using a set of optical density filters. The EQE measurement took place using Lasing IPCE-DC model with the series number LS1109-232 under a forward-wavelength sweep direction from 300 nm to 800 nm. The PL measurement was carried out on a Fluorolog Horiba Jobin Yvon spectrofluorimeter using 600 nm excitation wavelength. IS measurements were carried out under simulated AM 1.5G illumination using an HP-4192A impedance analyzer. Impedance data were extracted at three different dc levels: short-circuit current point, near maximum power point, and close to open-circuit point, superimposing an ac signal with 5 mV amplitude in the frequency range between 5 Hz and 2 MHz. The IS experimental data were fitted using Ivium software analyzer. All devices were measured in a sealed holder in N₂ atmosphere. Furthermore, the impedance analyzer was used to measure the C – V at 1 kHz with the voltage range from –1 V to 1 V in the dark. The performance of the devices was tested both prior to and after the impedance measurements with no sign of degradation. Blend film morphologies' topography images were obtained by AFM in a tapping mode using silicon probes with a spring constant of 1–5 N m⁻¹ and a resonant frequency of 75 kHz. Molecular Imaging Pico SPM II instrument (pico+) software was used to analyze the surface morphology images. The absorbance spectra were collected by a UV–vis/near infrared (NIR) spectrometer at room temperature.

Supporting Information

Supporting Information is available from the Wiley Online Library or from the author.

Acknowledgements

E.M. and A.A.A.T. contributed equally to this work. A.A.A.T. acknowledges the financial support from the European Union's Horizon 2020 research and innovation programme under the Marie Skłodowska-Curie grant agreement no. 713679. In addition, E.M. acknowledges the Agency for

Management of University and Research Grants (AGAUR) for receiving the fund with grant number 2019 FL_B01102. This work was further supported by the Spanish Ministerio de Ciencia, Innovación y Universidades (MICINN/FEDER) RTI2018-094040-B-I00, by AGAUR ref. 2017-SGR-1527. The authors also acknowledge Dr. Maria Mendez for the photoluminescence measurement held in the Institute of Chemical Research of Catalonia, Barcelona Institute of Science and Technology (ICIQ-BIST).

Conflict of Interest

The authors declare no conflict of interest.

Data Availability Statement

Research data are not shared.

Keywords

binary heterojunctions, nonfullerenes, organic photovoltaics, solvent additives, ternary heterojunctions, thermal annealing

Received: June 30, 2021

Revised: July 18, 2021

Published online:

- [1] Y. Firdaus, V. M. Le Corre, J. I. Khan, Z. Kan, F. Laquai, P. M. Beaujuge, T. D. Anthopoulos, *Adv. Sci.* **2019**, *6*, 1802028.
- [2] Y. Cui, H. Yao, J. Zhang, K. Xian, T. Zhang, L. Hong, Y. Wang, Y. Xu, K. Ma, C. An, C. He, Z. Wei, F. Gao, J. Hou, *Adv. Mater.* **2020**, *32*, 1.
- [3] J. Lv, H. Tang, J. Huang, C. Yan, K. Liu, Q. Yang, D. Hu, R. Singh, J. Lee, S. Lu, G. Li, Z. Kan, *Energy Environ. Sci.* **2021**, *14*, 3044.
- [4] B. Kan, J. Zhang, F. Liu, X. Wan, C. Li, X. Ke, Y. Wang, H. Feng, Y. Zhang, G. Long, R. H. Friend, A. A. Bakulin, Y. Chen, *Adv. Mater.* **2018**, *30*, 1.
- [5] M. B. Upama, M. A. Mahmud, G. Conibeer, A. Uddin, *Sol. RRL* **2020**, *4*, 1.
- [6] Z. Liang, J. Tong, H. Li, Y. Wang, N. Wang, J. Li, C. Yang, Y. Xia, *J. Mater. Chem. A* **2019**, *7*, 15841.
- [7] H. W. Cheng, P. Raghunath, K. L. Wang, P. Cheng, T. Haung, Q. Wu, J. Yuan, Y. C. Lin, H. C. Wang, Y. Zou, Z. K. Wang, M. C. Lin, K. H. Wei, Y. Yang, *Nano Lett.* **2020**, *20*, 715.
- [8] N. Tokmoldin, S. M. Hosseini, M. Raoufi, L. Q. Phuong, O. J. Sandberg, H. Guan, Y. Zou, D. Neher, S. Shoaee, *J. Mater. Chem. A* **2020**, *8*, 7854.
- [9] J. Yuan, Y. Zhang, L. Zhou, G. Zhang, H. L. Yip, T. K. Lau, X. Lu, C. Zhu, H. Peng, P. A. Johnson, M. Leclerc, Y. Cao, J. Ulanski, Y. Li, Y. Zou, *Joule* **2019**, *3*, 1140.
- [10] Y. Cui, H. Yao, J. Zhang, K. Xian, T. Zhang, L. Hong, Y. Wang, Y. Xu, K. Ma, C. An, C. He, Z. Wei, F. Gao, J. Hou, *Adv. Mater.* **2020**, *32*, 1.
- [11] Y. Cui, H. Yao, L. Hong, T. Zhang, Y. Tang, B. Lin, K. Xian, B. Gao, C. An, P. Bi, W. Ma, J. Hou, *Natl. Sci. Rev.* **2020**, *7*, 1239.
- [12] H. Fu, Z. Wang, Y. Sun, *Sol. RRL* **2018**, *2*, 1.
- [13] W. Ye, Y. Yang, Z. Zhang, Y. Zhu, L. Ye, C. Miao, Y. Lin, S. Zhang, *Sol. RRL* **2020**, *2000258*, 1.
- [14] D. Wang, H. Liu, Y. Li, G. Zhou, L. Zhan, H. Zhu, X. Lu, H. Chen, C. Z. Li, *Joule* **2021**, *5*, 945.
- [15] T. Zhu, L. Zheng, Z. Xiao, X. Meng, L. Liu, L. Ding, X. Gong, *Sol. RRL* **2019**, *3*, 1.
- [16] Y. Tong, Z. Xiao, X. Du, C. Zuo, Y. Li, M. Lv, Y. Yuan, C. Yi, F. Hao, Y. Hua, T. Lei, Q. Lin, K. Sun, D. Zhao, C. Duan, X. Shao, W. Li,

- H. L. Yip, Z. Xiao, B. Zhang, Q. Bian, Y. Cheng, S. Liu, M. Cheng, Z. Jin, S. Yang, L. Ding, *Sci. China Chem.* **2020**, *63*, 758.
- [17] C. J. Brabec, M. Heeney, I. Mc Culloch, J. Nelson, *Chem. Soc. Rev.* **2011**, *40*, 1185.
- [18] M. B. Upama, N. K. Elumalai, M. A. Mahmud, M. Wright, D. Wang, C. Xu, A. Uddin, *Sol. Energy Mater. Sol. Cells* **2018**, *176*, 109.
- [19] J. Wu, J. Lee, Y. C. Chin, H. Yao, H. Cha, J. Luke, J. Hou, J. S. Kim, J. R. Durrant, *Energy Environ. Sci.* **2020**, *13*, 2422.
- [20] W. Ma, J. R. Tumbleston, M. Wang, E. Gann, F. Huang, H. Ade, *Adv. Energy Mater.* **2013**, *3*, 864.
- [21] J. Li, Y. Wang, Z. Liang, N. Wang, J. Tong, C. Yang, X. Bao, Y. Xia, *ACS Appl. Mater. Interfaces* **2019**, *11*, 7022.
- [22] Y. Ji, L. Xu, X. Hao, K. Gao, *Sol. RRL* **2020**, *4*, 1.
- [23] D. Huang, Y. Li, Z. Xu, S. Zhao, L. Zhao, J. Zhao, *Phys. Chem. Chem. Phys.* **2015**, *17*, 8053.
- [24] K. S. Wienhold, V. Körstgens, S. Grott, X. Jiang, M. Schwartzkopf, S. V. Roth, P. Müller-Buschbaum, *ACS Appl. Mater. Interfaces* **2019**, *11*, 42313.
- [25] M. Qin, P. Cheng, J. Mai, T. K. Lau, Q. Zhang, J. Wang, C. Yan, K. Liu, C. J. Su, W. You, X. Lu, X. Zhan, *Sol. RRL* **2017**, *1*, 1.
- [26] F. Jin, G. Ding, Y. Wang, J. Yuan, W. Guo, H. Yuan, C. Sheng, W. Ma, H. Zhao, *J. Phys. Chem. C* **2017**, *121*, 8804.
- [27] N. Adhikari, D. Khatiwada, A. Dubey, Q. Qiao, *J. Photonics Energy* **2015**, *5*, 057207.
- [28] D. Corzo, K. Almasabi, E. Bihar, S. Macphee, D. Rosas-Villalva, N. Gasparini, S. Inal, D. Baran, *Adv. Mater. Technol.* **2019**, *4*, 1.
- [29] H.-W. Cheng, A. Mohapatra, Y.-M. Chang, C.-Y. Liao, Y.-T. Hsiao, C.-H. Chen, Y.-C. Lin, S.-Y. Huang, B. Chang, Y. Yang, C.-W. Chu, K.-H. Wei, *ACS Appl. Mater. Interfaces* **2021**, *13*, 27227.
- [30] H. W. Cheng, C. Y. Juan, A. Mohapatra, C. H. Chen, Y. C. Lin, B. Chang, P. Cheng, H. C. Wang, C. W. Chu, Y. Yang, K. H. Wei, *Nano Lett.* **2021**, *21*, 2207.
- [31] S. Liu, J. Yuan, W. Deng, M. Luo, Y. Xie, Q. Liang, Y. Zou, Z. He, H. Wu, Y. Cao, *Nat. Photonics* **2020**, *14*, 300.
- [32] P. Xue, S. Dai, T. K. Lau, J. Yu, J. Zhou, Y. Xiao, K. Meng, Z. Xie, G. Lu, X. Lu, R. P. S. Han, X. Zhan, *Sol. RRL* **2020**, *4*, 1.
- [33] Y. C. Lin, Y. J. Lu, C. S. Tsao, A. Saeki, J. X. Li, C. H. Chen, H. C. Wang, H. C. Chen, D. Meng, K. H. Wu, Y. Yang, K. H. Wei, *J. Mater. Chem. A* **2019**, *7*, 3072.
- [34] Y. C. Lin, H. W. Cheng, Y. W. Su, B. H. Lin, Y. J. Lu, C. H. Chen, H. C. Chen, Y. Yang, K. H. Wei, *Nano Energy* **2018**, *43*, 138.
- [35] Y. C. Lin, Y. W. Su, J. X. Li, B. H. Lin, C. H. Chen, H. C. Chen, K. H. Wu, Y. Yang, K. H. Wei, *J. Mater. Chem. A* **2017**, *5*, 18053.
- [36] J. M. Jiang, M. C. Yuan, K. Dinakaran, A. Hariharan, K. H. Wei, *J. Mater. Chem. A* **2013**, *1*, 4415.
- [37] C. H. Chen, Y. J. Lu, Y. W. Su, Y. C. Lin, H. K. Lin, H. C. Chen, H. C. Wang, J. X. Li, K. H. Wu, K. H. Wei, *Org. Electron.* **2019**, *7*, 185.
- [38] N. Gasparini, X. Jiao, T. Heumueller, D. Baran, G. J. Matt, S. Fladischer, E. Spiecker, H. Ade, C. J. Brabec, T. Ameri, *Nat. Energy* **2016**, *1*, 16118.
- [39] B. H. Jiang, Y. P. Wang, C. Y. Liao, Y. M. Chang, Y. W. Su, R. J. Jeng, C. P. Chen, *ACS Appl. Mater. Interfaces* **2021**, *13*, 1076.
- [40] T. Ameri, J. Min, N. Li, F. Machui, D. Baran, M. Forster, K. J. Schottler, D. Dolfen, U. Scherf, C. J. Brabec, *Adv. Energy Mater.* **2012**, *2*, 1198.
- [41] X. Ma, Y. Mi, F. Zhang, Q. An, M. Zhang, Z. Hu, X. Liu, J. Zhang, W. Tang, *Adv. Energy Mater.* **2018**, *8*, 1702854.
- [42] J. Yao, B. Qiu, Z. G. Zhang, L. Xue, R. Wang, C. Zhang, S. Chen, Q. Zhou, C. Sun, C. Yang, M. Xiao, L. Meng, Y. Li, *Nat. Commun.* **2020**, *11*, 1.
- [43] Y. Cui, H. Yao, J. Zhang, T. Zhang, Y. Wang, L. Hong, K. Xian, B. Xu, S. Zhang, J. Peng, Z. Wei, F. Gao, J. Hou, *Nat. Commun.* **2019**, *10*, 1.
- [44] V. S. Balderrama, J. G. Sánchez, G. Lastra, W. Cambarau, S. Arias, J. Pallarès, E. Palomares, M. Estrada, L. F. Marsal, *J. Mater. Chem. A* **2018**, *6*, 22534.
- [45] P. Yin, L. Wang, J. Liang, Y. Yu, L. Chen, C. Weng, C. Cui, P. Shen, *J. Mater. Chem. C* **2020**, *8*, 11223.
- [46] N. K. Elumalai, A. Uddin, *Energy Environ. Sci.* **2016**, *9*, 391.
- [47] J. D. Servaites, M. A. Ratner, T. J. Marks, *Energy Environ. Sci.* **2011**, *4*, 4410.
- [48] X. Wang, L. Zhang, L. Hu, Z. Xie, H. Mao, L. Tan, Y. Zhang, Y. Chen, *Adv. Funct. Mater.* **2021**, 2102291, <https://doi.org/10.1002/adfm.202102291>.
- [49] L. Zhan, S. Li, T. K. Lau, Y. Cui, X. Lu, M. Shi, C. Z. Li, H. Li, J. Hou, H. Chen, *Energy Environ. Sci.* **2020**, *13*, 635.
- [50] B. Du, J. Yi, H. Yan, T. Wang, *Chem. Eur. J.* **2021**, *27*, 2908.
- [51] Y. A. M. Ismail, T. Soga, T. Jimbo, *J. Appl. Phys.* **2011**, *109*, 1.
- [52] H. Jin, Y. Hou, F. Teng, P. Kopola, M. Tuomikoski, A. Maaninen, *Sol. Energy Mater. Sol. Cells* **2009**, *93*, 289.
- [53] A. Armin, M. Velusamy, P. Wolfert, Y. Zhang, P. L. Burn, P. Meredith, A. Pivrikas, *ACS Photonics* **2014**, *1*, 173.
- [54] F. Urbach, *Phys. Rev.* **1953**, *92*, 1324.
- [55] S. R. Cowan, A. Roy, A. J. Heeger, *Phys. Rev. B: Condens. Matter Mater. Phys.* **2010**, *82*, 1.
- [56] P. Hartnagel, T. Kirchartz, *Adv. Theory Simul.* **2020**, *3*, 1.
- [57] C. M. Proctor, T. Q. Nguyen, *Appl. Phys. Lett.* **2015**, *106*, 083301.
- [58] G. Juka, K. Arlauskas, *Sol. Energy* **2010**, <https://doi.org/10.5772/8072>.
- [59] Z. Liu, N. Wang, *J. Mater. Chem. C* **2019**, *7*, 10039.
- [60] V. Gupta, A. K. K. Kyaw, D. H. Wang, S. Chand, G. C. Bazan, A. J. Heeger, *Sci. Rep.* **2013**, *3*, 6.
- [61] C. Xiong, J. Sun, H. Yang, H. Jiang, *Sol. Energy* **2019**, *178*, 193.
- [62] V. D. Mihailetschi, L. J. A. Koster, P. W. M. Blom, C. Melzer, B. De Boer, J. K. J. Van Duren, R. A. J. Janssen, *Adv. Funct. Mater.* **2005**, *15*, 795.
- [63] V. D. Mihailetschi, L. J. A. Koster, J. C. Hummelen, P. W. M. Blom, *Phys. Rev. Lett.* **2004**, *93*, 19.
- [64] J.-L. Wu, F.-C. Chen, Y.-S. Hsiao, F.-C. Chien, P. Chen, C.-H. Kuo, M. H. Huang, C.-S. Hsu, *ACS Nano* **2011**, *5*, 959.
- [65] B. H. Jiang, Y. P. Wang, C. Y. Liao, Y. M. Chang, Y. W. Su, R. J. Jeng, C. P. Chen, *ACS Appl. Mater. Interfaces* **2021**, *13*, 1076.
- [66] J. Zhao, Y. Li, H. Lin, Y. Liu, K. Jiang, C. Mu, T. Ma, J. Y. Lin Lai, H. Hu, D. Yu, H. Yan, *Energy Environ. Sci.* **2015**, *8*, 520.
- [67] M. A. Pan, T. K. Lau, Y. Tang, Y. C. Wu, T. Liu, K. Li, M. C. Chen, X. Lu, W. Ma, C. Zhan, *J. Mater. Chem. A* **2019**, *7*, 20713.
- [68] A. A. A. Torimtumun, J. Follana-Berná, J. G. Sánchez, J. Pallarès, Á. Sastre-Santos, L. F. Marsal, *ACS Appl. Energy Mater.* **2021**, *4*, 5201.
- [69] H. Fu, W. Gao, Y. Li, F. Lin, X. Wu, J. H. Son, J. Luo, H. Y. Woo, Z. Zhu, A. K. Y. Jen, *Small Methods* **2020**, *4*.
- [70] A. G. Gaborik, J. W. Mohin, T. Kowalewski, G. R. Hutchison, *Adv. Funct. Mater.* **2015**, *25*, 1996.
- [71] G. Zhang, X. K. Chen, J. Xiao, P. C. Y. Chow, M. Ren, G. Kupgan, X. Jiao, C. C. S. Chan, X. Du, R. Xia, Z. Chen, J. Yuan, Y. Zhang, S. Zhang, Y. Liu, Y. Zou, H. Yan, K. S. Wong, V. Coropceanu, N. Li, C. J. Brabec, J. L. Bredas, H. L. Yip, Y. Cao, *Nat. Commun.* **2020**, *11*.
- [72] T. Kim, J. H. Kim, T. E. Kang, C. Lee, H. Kang, M. Shin, C. Wang, B. Ma, U. Jeong, T. S. Kim, B. J. Kim, *Nat. Commun.* **2015**, *6*, 1.
- [73] E. Von Hauff, *J. Phys. Chem. C* **2019**, *123*, 11329.

- [74] B. Arredondo, M. B. Martín-López, B. Romero, R. Vergaz, P. Romero-Gomez, J. Martorell, *Sol. Energy Mater. Sol. Cells* **2016**, *144*, 422.
- [75] E. Moustafa, J. G. Sánchez, L. F. Marsal, J. Pallarès, *ACS Appl. Energy Mater.* **2021**, *4*, 4099.
- [76] Z. He, K. Huang, C. Guo, Z. Jin, C. Hou, *AIP Adv.* **2019**, *9*, 045321.
- [77] H. Schroeder, *J. Appl. Phys.* **2015**, *117*, 215103.
- [78] S. S. Hegedus, E. A. Fagen, *J. Appl. Phys.* **1992**, *71*, 5941.
- [79] S. Wang, P. Kaienburg, B. Klingebiel, D. Schillings, T. Kirchartz, *J. Phys. Chem. C* **2018**, *122*, 9795.
- [80] B. Ecker, J. C. Nolasco, J. Pallarés, L. F. Marsal, J. Posdorfer, J. Parisi, E. Von Hauff, *Adv. Funct. Mater.* **2011**, *21*, 2705.
- [81] H. F. Haneef, A. M. Zeidell, O. D. Jurchescu, *J. Mater. Chem. C* **2020**, *8*, 759.
- [82] T. Walter, R. Herberholz, C. Müller, H. W. Schock, *J. Appl. Phys.* **1996**, *80*, 4411.
- [83] G. Garcia-Belmonte, A. Munar, E. M. Barea, J. Bisquert, I. Ugarte, R. Pacios, *Org. Electron.* **2008**, *9*, 847.
- [84] J. Bhattacharya, P. H. Joshi, R. Biswas, V. L. Dalal, *Solar Energy Materials and Solar Cells* **2017**, *164*, 70.
- [85] J. Wu, J. Luke, H. K. H. Lee, P. Shakya Tuladhar, H. Cha, S. Y. Jang, W. C. Tsoi, M. Heeney, H. Kang, K. Lee, T. Kirchartz, J. S. Kim, J. R. Durrant, *Nat. Commun.* **2019**, *10*, 1.
- [86] A. A. A. Torimtubun, J. G. Sánchez, J. Pallarès, L. F. Marsal, *Sustainable Energy Fuels* **2020**, *4*, 3378.
- [87] R. C. I. Mackenzie, V. S. Balderrama, S. Schmeisser, R. Stoof, S. Greedy, J. Pallarès, L. F. Marsal, A. Chanaewa, E. Von Hauff, *Adv. Energy Mater.* **2016**, *6*, 2.